Journal of Advanced Ceramics
2021, **10**(4): 778–789
https://doi.org/10.1007/s40145-021-0472-3
ISSN 2226-4108
CN 10-1154/TQ

Research Article

Effects of $(Mg_{1/3}Sb_{2/3})^{4+}$ substitution on the structure and microwave dielectric properties of $Ce_2Zr_3(MoO_4)_9$ ceramics

Xu ZHOU[a], Lintao LIU[a], Jiajia SUN[b], Ningkang ZHANG[b], Huazhang SUN[b], Haitao WU[a,*], Wenhong TAO[b,*]

[a]*School of Environmental and Material Engineering, Yantai University, Yantai 264005, China*
[b]*School of Materials Science and Engineering, University of Jinan, Jinan 250022, China*

Received: November 2, 2020; Revised: January 19, 2021; Accepted: March 6, 2021

Abstract: $Ce_2[Zr_{1-x}(Mg_{1/3}Sb_{2/3})_x]_3(MoO_4)_9$ ($0.02 \leqslant x \leqslant 0.10$) ceramics were prepared by the traditional solid-state method. A single phase, belonging to the space group of $R\bar{3}c$, was detected by using X-ray diffraction at the sintering temperatures ranging from 700 to 850 ℃. The microstructures of samples were examined by applying scanning electron microscopy (SEM). The crystal structure refinement of these samples was investigated in detail by performing the Rietveld refinement method. The intrinsic properties were calculated and explored via far-infrared reflectivity spectroscopy. The correlations between the chemical bond parameters and microwave dielectric properties were calculated and analyzed by Phillips–van Vechten–Levine (P–V–L) theory. $Ce_2[Zr_{0.94}(Mg_{1/3}Sb_{2/3})_{0.06}]_3(MoO_4)_9$ ceramics with excellent dielectric properties were sintered at 725 ℃ for 6 h (ε_r = 10.37, $Q\times f$ = 71,748 GHz, and τ_f = −13.6 ppm/℃, ε_r is the dielectric constant, $Q\times f$ is the quality factor, and τ_f is the temperature coefficient of resonant frequency).

Keywords: crystal structure; Phillips–van Vechten–Levine (P–V–L) theory; microwave dielectric property; $(Mg_{1/3}Sb_{2/3})$ doping

1 Introduction

It is well-known that dielectric materials have developed rapidly in the past decades. Microwave dielectric ceramics have sprung up in the communication industry and received widely attentions. It is required to have a high-quality factor ($Q\times f$), a moderate dielectric constant (ε_r), and a near-zero temperature coefficient of resonant frequency (τ_f) to meet the demands of applications [1,2]. Recently, researchers focused on novel microwave dielectric ceramics. At the same time, some researchers have widely investigated the substitution of cationic and composite ceramics to improve the dielectric properties of microwave dielectric materials [3–5]. In addition, high cost limits the application of these ceramics, and consequently it is required to reduce their sintering temperatures. The low temperature co-fired ceramic (LTCC) [6–8] technology has become a common method due to its simplicity and high efficiency. Hence, LTCC technology is becoming more and more important in practical applications.

In recent years, Mo-based microwave dielectric ceramics have been studied in depth as shown in Table 1 [9–13]. Many microwave dielectric ceramic systems

* Corresponding authors.
E-mail: H. Wu, mse_wuht@ujn.edu.cn;
W. Tao, mse_taowh@ujn.edu.cn

Table 1 Summarized microwave dielectric properties of Mo-based microwave dielectric ceramics

Material	Sintering temperature (℃)	ε_r	$Q\times f$ (GHz)	τ_f (ppm/℃)	Ref.
$Sm_2Zr_3(MoO_4)_9$	875	11.0	74,012	−45.3	[9]
$Nd_2Zr_3(MoO_4)_9$	850	10.8	58,942	−40.9	[9]
$Eu_2Zr_3(MoO_4)_9$	600	10.75	74,900	−8.88	[10]
$La_2Zr_3(MoO_4)_9$	650	10.8	61,790	−29.1	[11]
$La_2(Zr_{0.92}Ti_{0.08})_3(MoO_4)_9$	750	10.33	80,658	3.48	[11]
$Ce_2Zr_3(MoO_4)_9$	575	10.69	19,062	−1.29	[12]
$Ce_2(Zr_{0.92}Ti_{0.08})_3(MoO_4)_9$	775	11.28	84,200	−7.86	[13]
$Ce_2[Zr_{0.94}(Mg_{1/3}Sb_{2/3})_{0.06}]_3(MoO_4)_9$	725	10.37	71,748	−13.6	This work

have been developed, but their properties are not optimistic. The performance ($Q\times f$ = 19,062 GHz) of $Ce_2Zr_3(MoO_4)_9$ ceramic was investigated [12]. In order to improve $Q\times f$ of $Ce_2Zr_3(MoO_4)_9$ ceramics, doping $(Mg_{1/3}Sb_{2/3})^{4+}$ at Zr-sites was reported in this work. The crystal structure and the sintering behavior of samples were discussed in detail. Also, the relationship between the dielectric properties and the structure of samples was explored scientifically by far infrared reflectivity spectrum and the Phillips–van Vechten–Levine (P–V–L) theory.

2 Experimental

Highly pure powders of CeO_2, ZrO_2, MoO_3, MgO, and Sb_2O_5 were weighed accurately based on the stoichiometric composition of $Ce_2[Zr_{1-x}(Mg_{1/3}Sb_{2/3})_x]_3(MoO_4)_9$ ($0.02 \leqslant x \leqslant 0.10$). The mixed powders were continuously rotated for 24 h with ethanol media and ZrO_2 balls. Mixtures were oven-dried at 80 ℃ and pre-sintered at 700 ℃ for 2 h, and after that, ball milled and dried again under the same condition as above. Subsequently, the combination of powders and 10 wt% paraffin passed through a 60-mesh sieve, and a certain size of the cylinders (length ≈ 6 mm, diameter ≈ 10 mm) was pressed at 200 MPa. Those pressed cylinders were sintered from 700 to 850 ℃ for 6 h.

Phase identification of sintered pellets was analyzed using a X-ray diffraction (D8 Advance, Bruker Co., Germany) with Cu Kα radiation and refined lattice parameters were obtained using a FULLPROF program to explore structure. The surface microstructures of specimens were observed by using a QUANTA 250FEG type scanning electron microscope (SEM, FEI Co., USA), equipped with the energy dispersive spectrometer (EDS). The apparent densities of specimens were analyzed using Archimedes method. The infrared reflectivity spectrum was recorded by a Bruker IFS66v FTIR spectrometer at National Synchrotron Radiation Laboratory (NSRL, BL01B infrared beamline station, University of Science and Technology of China, China). In addition, dielectric behaviors were surveyed by employing the $TE_{01\delta}$ cavity method with a network analyzer (N5234A, Agilent Co., USA) and the Hakki–Coleman dielectric resonator method. The τ_f value was acquired by Eq. (1):

$$\tau_f = \frac{f_T - f_0}{60\times f_0}\times 10^6 \text{ (ppm/℃)} \quad (1)$$

where f_T and f_0 represent resonant frequencies at 85 and 25 ℃, respectively.

Relative density ($\rho_{relative}$) was applied via the following equations:

$$\rho_{theory} = \frac{ZA}{V_m N_A} \text{ (g/cm}^3\text{)} \quad (2)$$

$$\rho_{relative} = \frac{\rho_{apparent}}{\rho_{theory}}\times 100\% \quad (3)$$

where Z is the number of molecules, N_A refers to Avogadro constant, A represents the relative atomic weight, and V_m represents the unit cell volume.

3 Results and discussion

As shown in Fig. 1, the X-ray diffraction patterns of $Ce_2[Zr_{1-x}(Mg_{1/3}Sb_{2/3})_x]_3(MoO_4)_9$ ($0.02 \leqslant x \leqslant 0.10$) ceramics are sintered under different temperatures for 6 h. A single phase was detected in all samples. The peaks of sintered ceramics assigned to the standard data for $Pr_2Zr_3(MoO_4)_9$ (JCPDS No. 52-0688), which

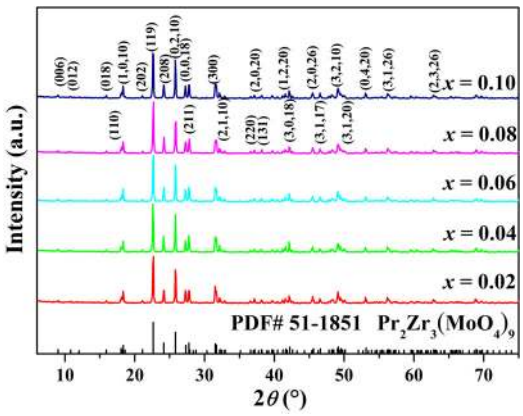

Fig. 1 XRD patterns of $Ce_2[Zr_{1-x}(Mg_{1/3}Sb_{2/3})_x]_3(MoO_4)_9$ (x = 0.02, 0.04, 0.06, 0.08, and 0.10) ceramics sintered at the densification temperature for 6 h.

indicated that the $Pr_2Zr_3(MoO_4)_9$-like crystal structure with a $R\bar{3}c$ space group was obtained. According to the result, the composition of the crystal phase is not changed by the content of $(Mg_{1/3}Sb_{2/3})^{4+}$ ions substitution [14]. In order to meet the needs of calculating density and complex chemical bonds, the structure, lattice parameters, bond length, and unit cell volumes were further analyzed and obtained by Rietveld refinement [15]. $Nd_2Zr_3(MoO_4)_9$ was chosen as the original model via FULLPROF program. Refinement plot of $Ce_2[Zr_{1-x}(Mg_{1/3}Sb_{2/3})_x]_3(MoO_4)_9$ ($0.02 \leqslant x \leqslant 0.10$) ceramics are displayed in Fig. 2, in which the observed values are expressed by red points, the calculated values are expressed by the black line, and different values between the observed and the calculated data are expressed by the blue curve. Obviously, excellent agreement is shown between the fitted values and the measured values. In addition, the refined discrepancy factors (R_{wp}, R_p, and χ^2), V_m, and lattice parameters of

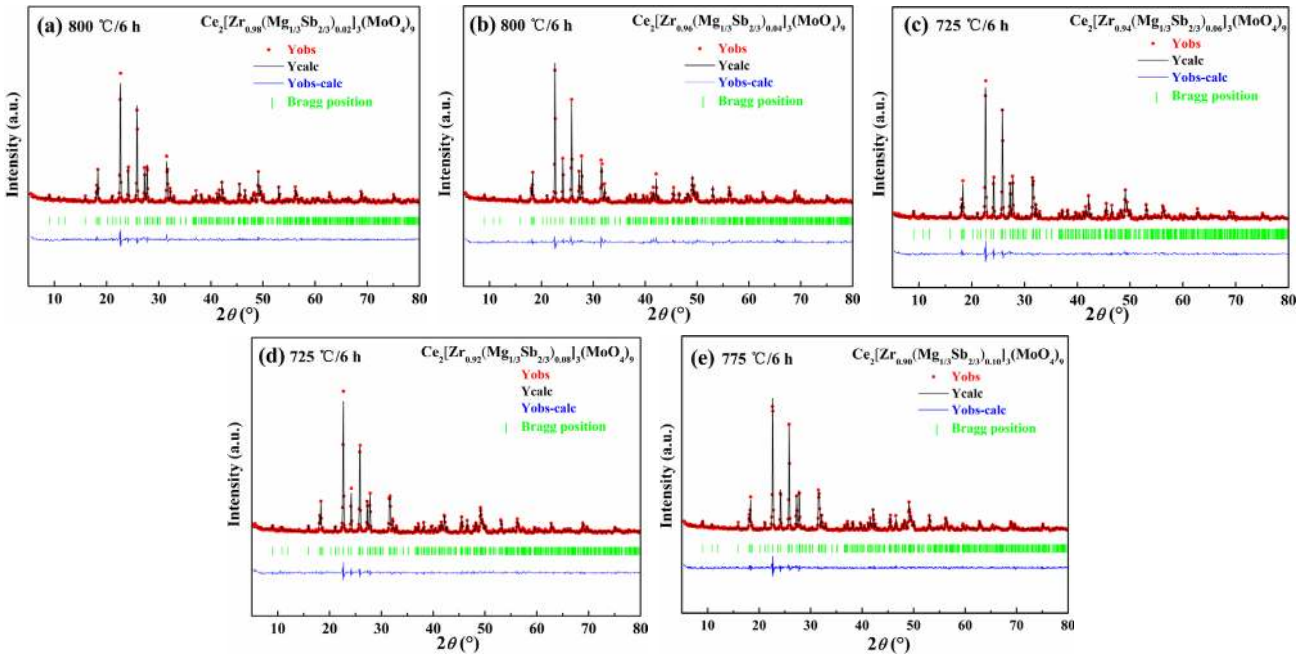

Fig. 2 Refinement results of $Ce_2[Zr_{1-x}(Mg_{1/3}Sb_{2/3})_x]_3(MoO_4)_9$ ceramics calcined under various conditions as indicated: (a) x = 0.02, (b) x = 0.04, (c) x = 0.06, (d) x = 0.08, and (e) x = 0.10.

Table 2 Refinement parameters of $Ce_2[Zr_{1-x}(Mg_{1/3}Sb_{2/3})_x]_3(MoO_4)_9$ ceramics sintered at the optimized sintering temperature

Structural parameter	$Ce_2[Zr_{1-x}(Mg_{1/3}Sb_{2/3})_x]_3(MoO_4)_9$				
	x = 0.02	x = 0.04	x = 0.06	x = 0.08	x = 0.10
$a = b$ (Å)	9.8344(1)	9.8333(0)	9.8310(9)	9.8288(2)	9.8254(1)
c (Å)	58.8580(5)	58.8603(6)	58.8723(1)	58.8835(0)	58.8729(0)
$\alpha = \beta$ (°)	90	90	90	90	90
γ (°)	120	120	120	120	120
V_m (Å^3)	4929.84(0)	4928.92(1)	4928.30(5)	4926.38(1)	4922.07(5)
R_p (%)	8.33	8.52	6.60	7.62	7.46
R_{wp} (%)	10.60	11.10	10.50	9.60	9.51
χ^2	2.04	2.23	1.90	1.70	1.71

R_p—the reliability factor of patterns; R_{wp} — the reliability factor of weighted patterns; χ^2—the goodness of fit indicator = chi^2 = $(R_{wp}/R_{exp})^2$.

all specimens are listed in Table 2. The R_{wp}, R_p, and χ^2 values were obtained in the range of 9.6%–11.1%, 6.6%–8.6%, and 1.70–2.23, respectively, indicating all the refinement results are acceptable and accurate.

With the amount of $(Mg_{1/3}Sb_{2/3})^{4+}$ increasing, the linear variation in lattice parameters (*a*, *b*, and *c*) and V_m are presented in Fig. 3. The lattice parameter *c* is linearly increased, but *a*, *b*, and V_m are linearly decreased correspondingly along with the augment of $(Mg_{1/3}Sb_{2/3})^{4+}$ because the ionic radius of Zr^{4+} (0.72 Å) is longer than that of $(Mg_{1/3}Sb_{2/3})^{4+}$ (0.64 Å) [16,17]. The schematic illustration (Fig. 4) and the refined atomic positions (Table 3) of $Ce_2[Zr_{1-x}(Mg_{1/3}Sb_{2/3})_x]_3(MoO_4)_9$ samples are exhibited clearly. The crystal structure of ceramics is composed of CeO_9, $Zr/Mg/SbO_6$, and MoO_4 polyhedra with common vertex angle.

The apparent densities of $Ce_2[Zr_{1-x}(Mg_{1/3}Sb_{2/3})_x]_3(MoO_4)_9$ ($0.02 \leqslant x \leqslant 0.10$) ceramics as a function of the sintering temperature are illustrated in Fig. 5. As the temperature increases, the apparent densities of each composition increase at first and then decrease slightly. For example, the apparent density of $Ce_2[Zr_{0.94}(Mg_{1/3}Sb_{2/3})_{0.06}]_3(MoO_4)_9$ ceramics increases from 3.71 to 3.83 g/cm^3, and then the apparent density drops to 3.81 g/cm^3 at 800 ℃. In general, an appropriate sintering temperature plays a vital role in the densification of the sample. The higher sintering temperature will accelerate the growth of crystal grains, and the pores will not be discharged in time, resulting in a poor densification sample. The maximum relative density of each composition is embedded in Fig. 5 as a function of $(Mg_{1/3}Sb_{2/3})^{4+}$ substitution. The apparent densities of the major sample were approximately 3.80 g/cm^3 and the $\rho_{relative}$ also has reached more than 95%. It is noticeable that the good degree of densification was in accord with the SEM results. Figures 6(a)–6(e) depict the SEM microphotographs of the specimens at their optimal temperatures. It is quite clear that the dense microstructure and unambiguous grain boundary of the specimens can be observed. As provided in Fig. 6(f), EDS of $Ce_2[Zr_{0.94}(Mg_{1/3}Sb_{2/3})_{0.06}]_3(MoO_4)_9$ ceramics is gained at 725 ℃ for 6 h. Atom ratios of O, Mo, Zr, Ce, Sb, and Mg are 73.56%, 16.91%, 5.93%, 3.48%, 0.07%,

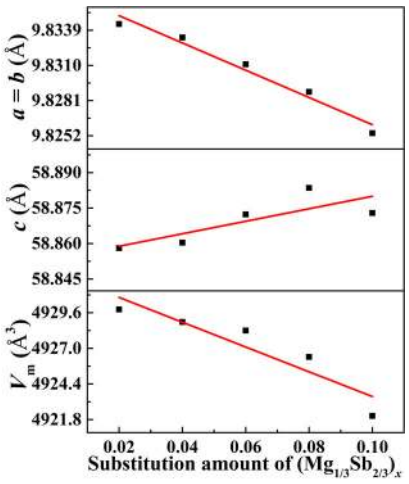

Fig. 3 *a*, *b*, *c*, and V_m of $Ce_2[Zr_{1-x}(Mg_{1/3}Sb_{2/3})_x]_3(MoO_4)_9$ ceramics as a function of the substitution amount of $(Mg_{1/3}Sb_{2/3})^{4+}$.

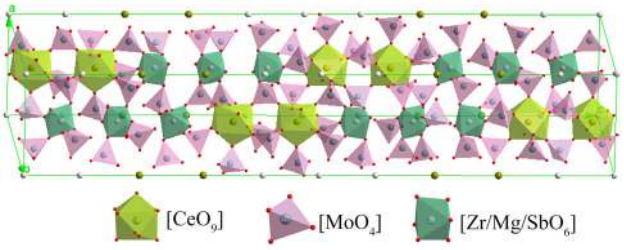

Fig. 4 Schematic illustration of $Ce_2[Zr_{1-x}(Mg_{1/3}Sb_{2/3})_x]_3(MoO_4)_9$ ceramics.

Table 3 Refined atomic positions of $Ce_2[Zr_{1-x}(Mg_{1/3}Sb_{2/3})_x]_3(MoO_4)_9$ samples

Atom	Wyckoff position	Site	*x*	*y*	*z*	Occupancy
Ce	12c	3	0.6667	0.3333	0.0297	0.3333
Zr1	6b	−3	0.0000	0.0000	0.0000	0.1667
Zr2	12c	3	0.3333	0.6667	0.0712	0.3333
Mo1	36f	1	0.0982	0.7275	0.0250	1.0000
Mo2	18e	2	0.2834	0.2834	0.2500	0.5000
O1	36f	1	−0.0959	0.5941	0.0308	1.0000
O2	36f	1	0.1628	0.6664	0.0027	1.0000
O3	36f	1	0.2061	0.7312	0.0500	1.0000
O4	36f	1	0.1192	0.9207	0.0201	1.0000
O5	36f	1	0.2879	0.4692	0.2456	1.0000
O6	36f	1	0.1708	0.1902	0.2729	1.0000

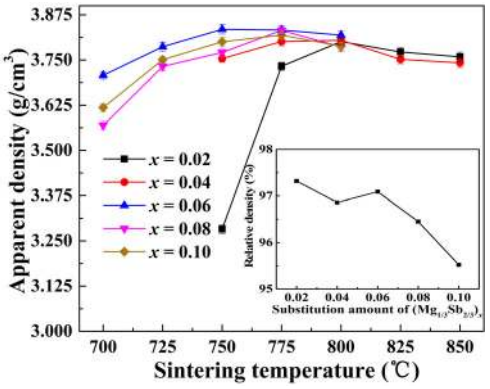

Fig. 5 Apparent densities of $Ce_2[Zr_{1-x}(Mg_{1/3}Sb_{2/3})_x]_3(MoO_4)_9$ ceramics as a function of the sintering temperature; the relative densities of each composition are shown in the inset.

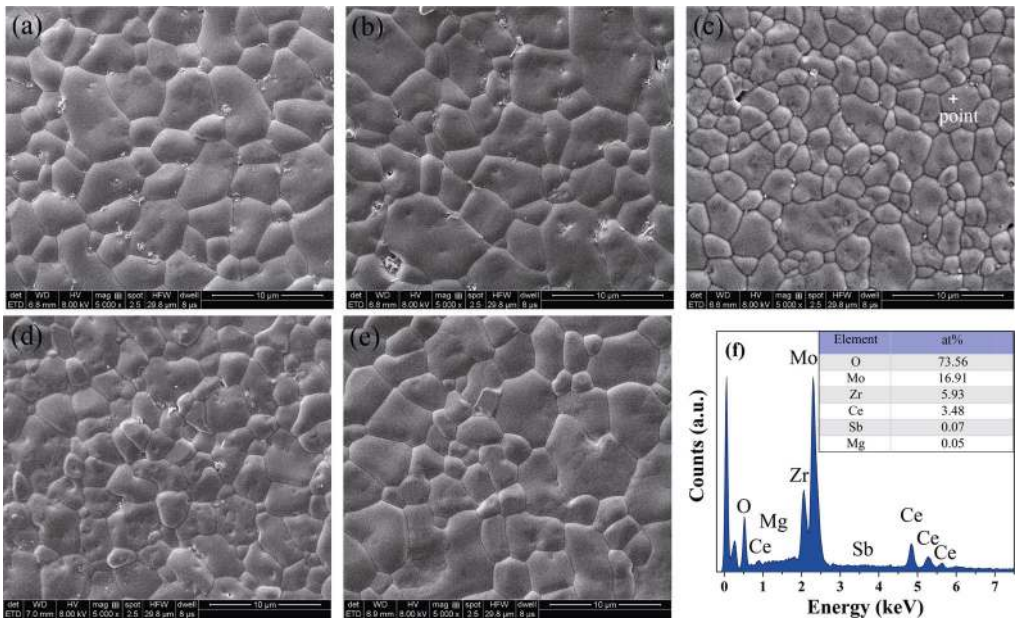

Fig. 6 SEM microphotographs of $Ce_2[Zr_{1-x}(Mg_{1/3}Sb_{2/3})_x]_3(MoO_4)_9$ ceramics at the densification temperature for 6 h: (a) x = 0.02, (b) x = 0.04, (c) x = 0.06, (d) x = 0.08, and (e) x = 0.10; (f) EDS analysis of $Ce_2[Zr_{0.94}(Mg_{1/3}Sb_{2/3})_{0.06}]_3(MoO_4)_9$ ceramics sintered at 725 ℃ for 6 h; the atom ratios of $Ce_2[Zr_{0.94}(Mg_{1/3}Sb_{2/3})_{0.06}]_3(MoO_4)_9$ ceramic is shown in the inset of Fig. 6(f).

and 0.05%, respectively, which are in consistent with the chemical formula.

The ε_r of ceramics with different $(Mg_{1/3}Sb_{2/3})^{4+}$ contents (x = 0.02, 0.04, 0.06, 0.08, and 0.10) as a function of the sintering temperature is revealed in Fig. 7(a). The factors that affect the ε_r are mainly divided into external parameters and intrinsic factors. Intrinsic factors include lattice structure and ionic polarizabilities, whereas external parameters include impurities, density, and second phase [18]. No secondary phase is detected in Fig. 1 and the lattice structure has no change. Thus, the ε_r of $Ce_2[Zr_{1-x}(Mg_{1/3}Sb_{2/3})_x]_3(MoO_4)_9$ ($0.02 \leqslant x \leqslant 0.10$) ceramics was determined mainly by the apparent density. Figure 5 shows that the apparent densities of the sample increased and then decreased slightly as the temperature increased. It was easy to notice that the ε_r existed almost similar trend with the apparent density, which indicated that the main contribution of the ε_r was the apparent density.

The $Q\times f$ of $Ce_2[Zr_{1-x}(Mg_{1/3}Sb_{2/3})_x]_3(MoO_4)_9$ ($0.02 \leqslant x \leqslant 0.10$) ceramics sintered at 700–850 ℃ for 6 h is plotted in Fig. 7(b). The quality factor depends on the presence of intrinsic and extrinsic dielectric losses at microwave frequencies. The extrinsic losses are dominated by porosity, secondary phase, and lattice defects, whereas the intrinsic loss is mainly contributed by lattice vibrational modes [19]. It was obvious that the $Q\times f$ of each composition existed similar trend, which increased firstly and then decreased. The optimal points of $Q\times f$ were presented at 800, 800, 725, 725, 725, and 775 ℃, In this study, the excellent

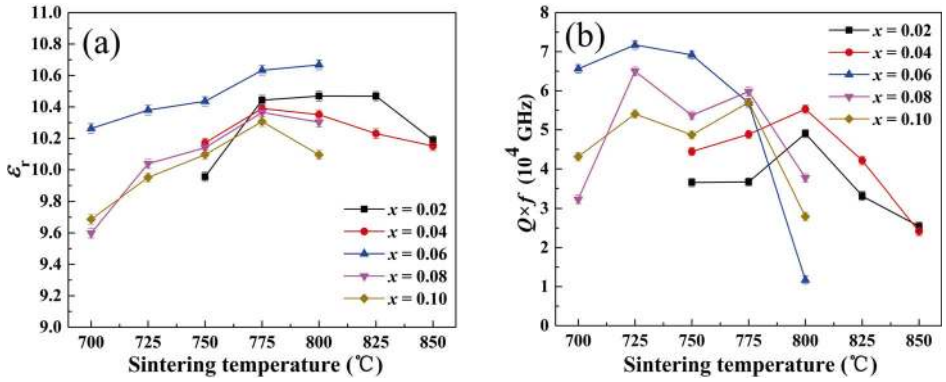

Fig. 7 (a) ε_r and (b) $Q\times f$ values of $Ce_2[Zr_{1-x}(Mg_{1/3}Sb_{2/3})_x]_3(MoO_4)_9$ ceramics sintered at 700–800 ℃.

properties of $Ce_2[Zr_{0.94}(Mg_{1/3}Sb_{2/3})_{0.06}]_3(MoO_4)_9$ ceramics (ε_r = 10.37, $Q\times f$ = 71,748 GHz, and τ_f = −13.6 ppm/℃) were obtained at 725 ℃ for 6 h. At the optimal sintering temperature, the quality factor of $Ce_2[Zr_{0.94}(Mg_{1/3}Sb_{2/3})_{0.06}]_3(MoO_4)_9$ ceramics has been greatly improved compared to previous reports, owing to the partial replacement of Zr^{4+} by $(Mg_{1/3}Sb_{2/3})^{4+}$ ions.

As we know, chemical bond theory of complex crystals was used to characterize the intrinsic relationships between chemical bond and crystal structure. Wu *et al*. [15] successfully generalized P–V–L theory, suggesting that the crystalline structure parameters could be calculated by chemical bond. Any complex crystal can be decomposed into multiple binary crystals. The bond equation of $Ce_2[Zr_{1-x}(Mg_{1/3}Sb_{2/3})_x]_3(MoO_4)_9$ ($0.02 \leqslant x \leqslant 0.10$) ceramics was shown in Eq. (4). In this work, the $Ce_2[Zr_{1-x}(Mg_{1/3}Sb_{2/3})_x]_3(MoO_4)_9$ ceramics are constituted of Ce–O, Zr(Mg/Sb)–O and Mo–O bonds. The effective valences of cations are P_{Ce} = 3, $P_{Zr(Mg/Sb)}$ = 4, and P_{Mo} = 6, and the valence of the oxygen ion follows Eq. (4). The effective valences in the Ce–O bond, Zr(Mg/Sb)–O bond, and Mo–O bond are $P_{O–Ce}$ = −2/3, $P_{O–Zr(Mg/Sb)}$ = −4/3, and $P_{O–Mo}$ = −3, respectively.

$$\begin{aligned}
&Ce_2[Zr_{1-x}(Mg_{1/3}Sb_{2/3})_x]_3(MoO_4)_9\\
&\rightarrow Ce_2 + Zr/(Mg_{1/3}Sb_{2/3})(1) + Zr/(Mg_{1/3}Sb_{2/3})(2)_2\\
&\quad + Mo(1)_6 + Mo(2)_3 + O(1)_6 + O(2)_6 + O(3)_6\\
&\quad + O(4)_6 + O(5)_6 + O(6)_6\\
&\rightarrow Ce_{2/3}O(1)_3 + Ce_{2/3}O(2)_3 + Ce_{2/3}O(6)_3\\
&\quad + Zr/(Mg_{1/3}Sb_{2/3})(1)O(4)_3 + Zr/(Mg_{1/3}Sb_{2/3})(2)O(3)_3\\
&\quad + Zr/(Mg_{1/3}Sb_{2/3})(2)O(5)_3 + Mo(1)_{3/2}O(1)_3\\
&\quad + Mo(1)_{3/2}O(2)_3 + Mo(1)_{3/2}O(3)_3 + Mo(1)_{3/2}O(4)_3\\
&\quad + Mo(2)_{3/2}O(5)_3 + Mo(2)_{3/2}O(6)_3
\end{aligned} \tag{4}$$

The bond ionicity (f_i) usually could be evaluated by using Eqs. (5)–(9) [15,20,21]:

$$\varepsilon_r = \frac{{n_0}^2 - 1}{1 - f_i} + 1 \tag{5}$$

$$f_i^{\mu} = \frac{(C^{\mu})^2}{(E_g^{\mu})^2} \tag{6}$$

$$(E_g^{\mu})^2 = (E_h^{\mu})^2 + (C^{\mu})^2 \tag{7}$$

$$(E_h^{\mu})^2 = \frac{39.74}{(d^{\mu})^{2.48}} \tag{8}$$

$$C^{\mu} = 14.4 b^{\mu} \exp(-k_s^{\mu} r_0^{\mu})[(Z_A^{\mu})^* - \frac{n}{m}(Z_B^{\mu})^*]/r_0^{\mu} \tag{9}$$

where d^{μ} and b^{μ} are the bond length and correction factor, respectively, $(Z_A^{\mu})^*$ is the effective number of valence electrons on cation A, $(Z_B^{\mu})^*$ is the effective number of valence electrons on anion B, n_0 represents the refractive index, r_0^{μ} is the average radius of A and B in angstroms, m and n are obtained from the binary crystal A_mB_n type compounds, E_g^{μ} represents the average energy gap, E_h^{μ} represents the homopolar part, f_i^{μ} is the bond ionicity of an individual bond μ, C^{μ} represents the heteropolar part, and $\exp(-k_s^{\mu} r_0^{\mu})$ is Thomas–Fermi screening factor [22].

The f_i is explored quantitatively as shown in Table 4. In addition, ε_r and an individual bond ionicity $f_{i(Mo1–O(2))}$ as a function of the content of $(Mg_{1/3}Sb_{2/3})^{4+}$ substitution are shown in Fig. 8. The ε_r values display a decreasing tendency from 10.47 to 10.03 along with the augment of $(Mg_{1/3}Sb_{2/3})^{4+}$. The positive correlation between relative permittivity and f_i is described in Eq. (5). As increasing of $(Mg_{1/3}Sb_{2/3})^{4+}$ content, $f_{i(Mo1–O(2))}$ and ε_r values show the same tendency, which indicate the ε_r values are strongly dependent on $f_{i(Mo1–O(2))}$.

Lattice energy can be used to predict and explain many physical and chemical properties of ionic crystals, so the larger the lattice energy, the more stable the structure. The lattice energy (U, Table 5) of specimen could be evaluated according to Eqs. (10)–(13) [15,20,21]. Figure 9 presents $U_{(Zr(Mg/Sb)1–O(4))}$ values and the quality factor $Q\times f$ as a variation of $(Mg_{1/3}Sb_{2/3})^{4+}$ substitution. The $Q\times f$ values increased from 49,033 to 64,012 GHz, and then decreased to 48,690 GHz. They all show the same trend of increasing first and then decreasing, indicating that $Q\times f$ is mainly affected by $U_{(Zr(Mg/Sb)1–O(4))}$.

$$U_{cal} = \sum_{\mu} U_b^{\mu} \tag{10}$$

$$U_b^{\mu} = U_{bc}^{\mu} + U_{bi}^{\mu} \tag{11}$$

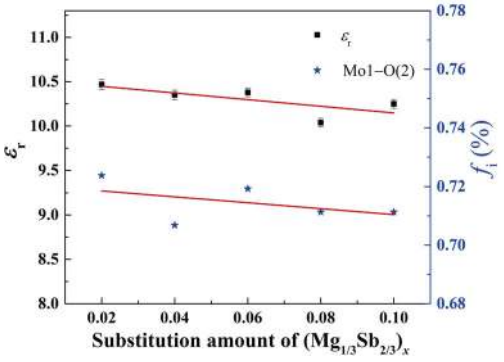

Fig. 8 ε_r and the Mo1–O(2) bond ionicity of $Ce_2[Zr_{1-x}(Mg_{1/3}Sb_{2/3})_x]_3(MoO_4)_9$ ceramics as a function of the content of $(Mg_{1/3}Sb_{2/3})^{4+}$ substitution.

Table 4 f_i of $Ce_2[Zr_{1-x}(Mg_{1/3}Sb_{2/3})_x]_3(MoO_4)_9$ (x = 0.02–0.10) ceramics sintered at the densification temperature for 6 h

$Ce_2[Zr_{1-x}(Mg_{1/3}Sb_{2/3})_x]_3(MoO_4)_9$	f_i (%)				
	x = 0.02	x = 0.04	x = 0.06	x = 0.08	x = 0.10
Ce–O(1)[1]	0.8484	0.8518	0.8467	0.8488	0.8491
Ce–O(1)[2]	0.8484	0.8518	0.8467	0.8489	0.8491
Ce–O(1)[3]	0.8485	0.8518	0.8467	0.8489	0.8491
Ce–O(2)[1]	0.8527	0.8527	0.8553	0.8561	0.8558
Ce–O(2)[2]	0.8527	0.8527	0.8553	0.8561	0.8558
Ce–O(2)[3]	0.8527	0.8527	0.8553	0.8561	0.8558
Ce–O(6)[1]	0.8523	0.8540	0.8524	0.8544	0.8520
Ce–O(6)[2]	0.8523	0.8540	0.8524	0.8544	0.8521
Ce–O(6)[3]	0.8523	0.8540	0.8524	0.8545	0.8521
Zr(Mg/Sb)1–O(4)×6	0.7964	0.7868	0.7851	0.7873	0.7880
Zr(Mg/Sb)2–O(3)[1]	0.7912	0.7757	0.8014	0.7895	0.7978
Zr(Mg/Sb)2–O(3)[2]	0.7912	0.7758	0.8015	0.7895	0.7978
Zr(Mg/Sb)2–O(3)[3]	0.7913	0.7758	0.8015	0.7895	0.7979
Zr(Mg/Sb)2–O(5)[1]	0.7849	0.7824	0.7920	0.7884	0.7891
Zr(Mg/Sb)2–O(5)[2]	0.7850	0.7824	0.7920	0.7884	0.7891
Zr(Mg/Sb)2–O(5)[3]	0.7850	0.7825	0.7920	0.7885	0.7892
Mo1–O(1)	0.7237	0.7167	0.7298	0.7194	0.7251
Mo1–O(2)	0.7237	0.7068	0.7193	0.7113	0.7113
Mo1–O(3)	0.7315	0.7344	0.7248	0.7348	0.7237
Mo1–O(4)	0.7369	0.7269	0.7474	0.7377	0.7363
Mo2–O(5)×2	0.7248	0.7344	0.7338	0.7381	0.7288
Mo2–O(6)×2	0.7276	0.7064	0.7268	0.7183	0.7258

Superscripts 1, 2, and 3 — three different bonds.

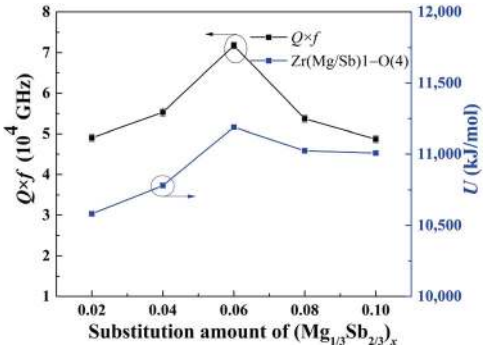

Fig. 9 $Q\times f$ and the Zr(Mg/Sb)1–O(4) lattice energy of $Ce_2[Zr_{1-x}(Mg_{1/3}Sb_{2/3})_x]_3(MoO_4)_9$ ceramics as a function of the content of $(Mg_{1/3}Sb_{2/3})^{4+}$ substitution.

$$U_{bc}^{\mu} = 2100m\frac{(Z_A^{\mu})^{1.64}}{(d^{\mu})^{0.75}}f_C^{\mu} \quad (12)$$

$$U_{bi}^{\mu} = 1270\frac{(m+n)Z_A^{\mu}Z_B^{\mu}}{d^{\mu}}\left(1-\frac{0.4}{d^{\mu}}\right)f_i^{\mu} \quad (13)$$

where U_{bi}^{μ} and U_{bc}^{μ} represent ionic energy part and covalent energy part, respectively. f_C^{μ} is the bond ionicity of an individual bond μ. Z_A^{μ} and Z_B^{μ} are the valence states of cation and anion, respectively, which constituted the μ bond.

Zhang *et al*. [23,24] had reported a strong relationship between bond energy E and τ_f, which a smaller $|\tau_f|$ corresponds to a higher bond energy value. The E value of an individual bond μ could be calculated by Eqs. (14)–(18) [25–27]:

$$E^{\mu} = t_c E_c^{\mu} + t_i E_i^{\mu} \quad (14)$$

$$E_c^{\mu} = \frac{(r_{cA}+r_{cB})}{d^{\mu}}(E_{A-A}E_{B-B})^{1/2}\ (\text{kJ/mol}) \quad (15)$$

$$E_i^{\mu} = \frac{1389.088}{d^{\mu}}\ (\text{kJ/mol}) \quad (16)$$

$$t_i = \left|\frac{S_A - S_B}{6}\right| \quad (17)$$

$$t_c + t_i = 1 \quad (18)$$

where E^{μ} is bond energy for the type μ bond, which was composed of nonpolar covalence energy E_c^{μ} and

Table 5 *U* of $Ce_2[Zr_{1-x}(Mg_{1/3}Sb_{2/3})_x]_3(MoO_4)_9$ (x = 0.02–0.10) ceramics sintered at the densification temperature for 6 h

$Ce_2[Zr_{1-x}(Mg_{1/3}Sb_{2/3})_x]_3(MoO_4)_9$	*U* (kJ/mol)				
	x = 0.02	x = 0.04	x = 0.06	x = 0.08	x = 0.10
Ce–O(1)[1]	3364	3208	3413	3352	3354
Ce–O(1)[2]	3364	3207	3412	3351	3352
Ce–O(1)[3]	3364	3207	3412	3351	3352
Ce–O(2)[1]	3276	3188	3235	3200	3212
Ce–O(2)[2]	3276	3188	3234	3199	3212
Ce–O(2)[3]	3276	3188	3234	3199	3211
Ce–O(6)[1]	3285	3160	3296	3236	3291
Ce–O(6)[2]	3284	3160	3295	3235	3291
Ce–O(6)[3]	3284	3159	3295	3234	3291
Zr(Mg/Sb)1–O(4)×6	10,580	10,780	11,189	11,023	11,007
Zr(Mg/Sb)2–O(3)[1]	10,844	11,319	10,360	10,916	10,512
Zr(Mg/Sb)2–O(3)[2]	10,842	11,317	10,358	10,914	10,510
Zr(Mg/Sb)2–O(3)[3]	10,842	11,315	10,358	10,913	10,509
Zr(Mg/Sb)2–O(5)[1]	11,152	10,998	10,850	10,968	10,955
Zr(Mg/Sb)2–O(5)[2]	11,151	10,997	10,849	10,967	10,954
Zr(Mg/Sb)2–O(5)[3]	11,149	10,995	10,847	10,965	10,951
Mo1–O(1)	43,980	43,859	43,164	44,597	43,763
Mo1–O(2)	43,964	45,433	44,862	45,862	45,940
Mo1–O(3)	42,658	40,742	43,989	42,023	43,995
Mo1–O(4)	41,707	42,121	39,969	41,489	41,852
Mo2–O(5)×2	43,793	40,747	42,479	41,418	43,146
Mo2–O(6)×2	43,329	45,493	43,655	44,782	43,658

complete ionicity energy E_i^μ parts, S_A and S_B represent the electronegativity of ions, t_c and t_i are covalent and ionic blending coefficients, respectively, r_{cA} and r_{cB} are the covalent radii, and E_{A-A} and E_{B-B} are homonuclear bond energy [28].

The τ_f and an individual bond ionicity $E_{(Mo1-O(1))}$ as a function of the content of $(Mg_{1/3}Sb_{2/3})^{4+}$ substitution are illustrated in Fig. 10. In addition, the calculated E values are shown in Table 6. The τ_f values of ceramics fluctuated slightly between −8.59 and −13.69 ppm/℃ with $(Mg_{1/3}Sb_{2/3})^{4+}$ increasing in our experiments. The $E_{(Mo1-O(1))}$ and τ_f have the same trend, indicating that τ_f is mainly influenced by $E_{(Mo1-O(1))}$.

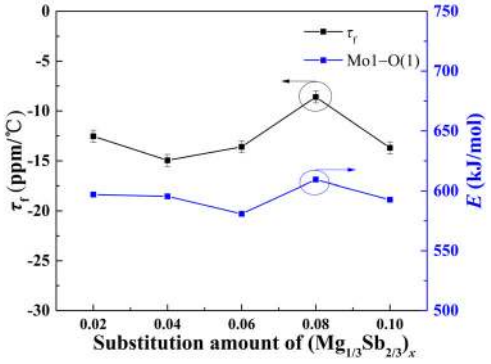

Fig. 10 τ_f and the Mo1–O(1) bond energy of $Ce_2[Zr_{1-x}(Mg_{1/3}Sb_{2/3})_x]_3(MoO_4)_9$ ceramics as a function of the content of $(Mg_{1/3}Sb_{2/3})^{4+}$ substitution.

The τ_f is obtained by Eq. (19) and the α is described via Eqs. (20)–(23):

$$\tau_f = -\left(\frac{\tau_\varepsilon}{2} + \alpha\right) \tag{19}$$

$$\alpha = \sum_\mu F_{mn}^\mu \alpha_{mn}^\mu \tag{20}$$

$$\alpha_{mn}^\mu = -3.1685 + 0.8376\gamma_{mn} \tag{21}$$

$$\gamma_{mn} = \frac{kZ_A^\mu N_{CA}^\mu}{U_b^\mu \Delta_A}\beta_{mn} \tag{22}$$

$$\beta_{mn} = \frac{m(m+n)}{2n} \tag{23}$$

where γ_{mn} is a parameter of the binary bonding formula, Δ_A is the periodic constant of cation, k is the Boltzmann constant, N_{CA}^μ represents the coordination

Table 6 E **of** $Ce_2[Zr_{1-x}(Mg_{1/3}Sb_{2/3})_x]_3(MoO_4)_9$ **(x = 0.02–0.10) ceramics sintered at the densification temperature for 6 h**

$Ce_2[Zr_{1-x}(Mg_{1/3}Sb_{2/3})_x]_3(MoO_4)_9$	E (kJ/mol)				
	x = 0.02	x = 0.04	x = 0.06	x = 0.08	x = 0.10
Ce–O(1)[1]	420.9821	397.1351	428.3333	419.0938	419.3161
Ce–O(1)[2]	420.8959	397.0431	428.2441	418.9913	419.2306
Ce–O(1)[3]	420.8097	396.9971	428.1549	418.9230	419.1622
Ce–O(2)[1]	407.8353	394.2862	401.9027	396.5835	398.4747
Ce–O(2)[2]	407.7868	394.2408	401.8555	396.5376	398.4283
Ce–O(2)[3]	407.7382	394.1954	401.8084	396.4917	398.3820
Ce–O(6)[1]	409.1178	390.1848	410.8842	401.8398	410.1627
Ce–O(6)[2]	409.0527	390.1552	410.8513	401.7927	410.1136
Ce–O(6)[3]	409.0038	390.0811	410.7692	401.7299	410.0482
Zr(Mg/Sb)1–O(4)×6	483.6989	494.9655	519.9098	509.8280	508.8463
Zr(Mg/Sb)2–O(3)[1]	499.2091	527.2509	470.9886	503.4523	479.7139
Zr(Mg/Sb)2–O(3)[2]	499.0641	527.0891	470.8595	503.3048	479.5799
Zr(Mg/Sb)2–O(3)[3]	499.0158	527.0352	470.8380	503.2557	479.5353
Zr(Mg/Sb)2–O(5)[1]	517.6120	507.9184	499.6205	506.5205	505.7748
Zr(Mg/Sb)2–O(5)[2]	517.5340	507.8684	499.5479	506.4707	505.7003
Zr(Mg/Sb)2–O(5)[3]	517.3781	507.7182	499.4268	506.3214	505.5515
Mo1–O(1)	597.0129	595.5327	580.8629	609.3766	592.6962
Mo1–O(2)	596.7025	627.2896	614.5251	635.2764	636.8040
Mo1–O(3)	571.2568	536.2299	597.0474	559.2248	597.2891
Mo1–O(4)	553.2635	561.9021	521.2639	549.2328	555.9438
Mo2–O(5)×2	593.3090	536.3134	567.7086	547.9217	580.6343
Mo2–O(6)×2	584.2142	628.5494	590.4598	613.1024	590.6287

number of cations, τ_ε is the temperature coefficient of the ε_r, and F_{mn}^{μ} represents the proportion of μ bond. Calculated thermal expansion coefficient α values are shown in Table 7. Obviously, the values of $\alpha_{Zr(Mg/Sb)-O}$ and α_{Ce-O} are positive. The values of α_{Mo-O} have a positive influence on τ_f because of $\alpha_{Mo-O} < 0$.

As is known, it is difficult to detect the intrinsic loss and extrinsic loss of microwave dielectric ceramics by conventional testing methods. Far-infrared spectral analysis can reflect the intrinsic loss to a certain extent. These spectra were analyzed by using the classical harmonic oscillator model that was applied to study infrared spectroscopy. It relies on two equations: The standard Lorentzian formula (Eq. (24)) and the Fresnel formula (Eq. (25)) [29,30]. The dielectric loss tangent tanδ is evaluated by Eq. (26).

$$\varepsilon^*(\omega) = \varepsilon_\infty + \sum_{j=1}^{n} \frac{\omega_{pj}^2}{\omega_{oj}^2 - \omega^2 + j\omega\gamma_j} \tag{24}$$

$$R = \left| \frac{1 - \sqrt{\varepsilon^*(\omega)}}{1 + \sqrt{\varepsilon^*(\omega)}} \right|^2 \tag{25}$$

$$\tan\delta = \frac{\varepsilon''}{\varepsilon'} = \frac{\sum_{j=1}^{n} \Delta\varepsilon_j (\gamma_j \omega) / \omega_{oj}^2}{\varepsilon_\infty + \sum_{j=1}^{n} \Delta\varepsilon_j} \tag{26}$$

where $\Delta\varepsilon_j$ is contribution from each mode, γ_j is the damping factor, ω is frequency, ε' and ε'' are the real part and imaginary parts of the permittivity, respectively, ε_∞ is the relative permittivity caused by electronic polarization, ω_{pj} is the plasma frequency, $\varepsilon^*(\omega)$ is the complex dielectric function, ω_{oj} is the transverse frequency, n is the number of transverse phonon modes, and R is the infrared reflectivity.

As shown in Fig. 11(a), the fitted infrared spectrum of the $Ce_2[Zr_{0.94}(Mg_{1/3}Sb_{2/3})_{0.06}]_3(MoO_4)_9$ sample is depicted. The fitted infrared reflectivity spectrum is in good agreement with the measured part. In addition, real and imaginary parts of the permittivity are given in Fig. 11(b). Table 8 lists the fitted phonon parameters, indicating they are fitted with 16 modes. As compared with the measured permittivity, the calculated one was slightly large. The measured value (1.35×10^{-4}) and

Table 7 α of $Ce_2[Zr_{1-x}(Mg_{1/3}Sb_{2/3})_x]_3(MoO_4)_9$ (x = 0.02–0.10) ceramics sintered at the densification temperature for 6 h

$Ce_2[Zr_{1-x}(Mg_{1/3}Sb_{2/3})_x]_3(MoO_4)_9$	α (10^{-6}/K)				
	x = 0.02	x = 0.04	x = 0.06	x = 0.08	x = 0.10
Ce–O(1)[1]	9.9082	10.5441	9.7205	9.9551	9.9472
Ce–O(1)[2]	9.9082	10.5484	9.7243	9.9590	9.9551
Ce–O(1)[3]	9.9082	10.5484	9.7243	9.9590	9.9551
Ce–O(2)[1]	10.2595	10.6302	10.4297	10.5784	10.5271
Ce–O(2)[2]	10.2595	10.6302	10.4339	10.5827	10.5271
Ce–O(2)[3]	10.2595	10.6302	10.4339	10.5827	10.5313
Ce–O(6)[1]	10.2227	10.7524	10.1780	10.4255	10.1983
Ce–O(6)[2]	10.2268	10.7524	10.1821	10.4297	10.1983
Ce–O(6)[3]	10.2268	10.7568	10.1821	10.4339	10.1983
Zr(Mg/Sb)1–O(4)×6	3.5771	3.4520	3.2100	3.3060	3.3154
Zr(Mg/Sb)2–O(3)[1]	3.4129	3.1367	3.7204	3.3695	3.6208
Zr(Mg/Sb)2–O(3)[2]	3.4141	3.1378	3.7217	3.3707	3.6220
Zr(Mg/Sb)2–O(3)[3]	3.4141	3.1389	3.7217	3.3713	3.6227
Zr(Mg/Sb)2–O(5)[1]	3.2311	3.3207	3.4093	3.3385	3.3462
Zr(Mg/Sb)2–O(5)[2]	3.2317	3.3213	3.4099	3.3391	3.3468
Zr(Mg/Sb)2–O(5)[3]	3.2329	3.3225	3.4111	3.3403	3.3486
Mo1–O(1)	−0.4301	−0.4225	−0.3783	−0.4680	−0.4165
Mo1–O(2)	−0.4291	−0.5177	−0.4839	−0.5425	−0.5469
Mo1–O(3)	−0.3452	−0.2125	−0.4307	−0.3026	−0.4310
Mo1–O(4)	−0.2809	−0.3092	−0.1553	−0.2657	−0.2909
Mo2–O(5)×2	−0.4184	−0.2128	−0.3333	−0.2607	−0.3772
Mo2–O(6)×2	−0.3890	−0.5212	−0.4097	−0.4791	−0.4099

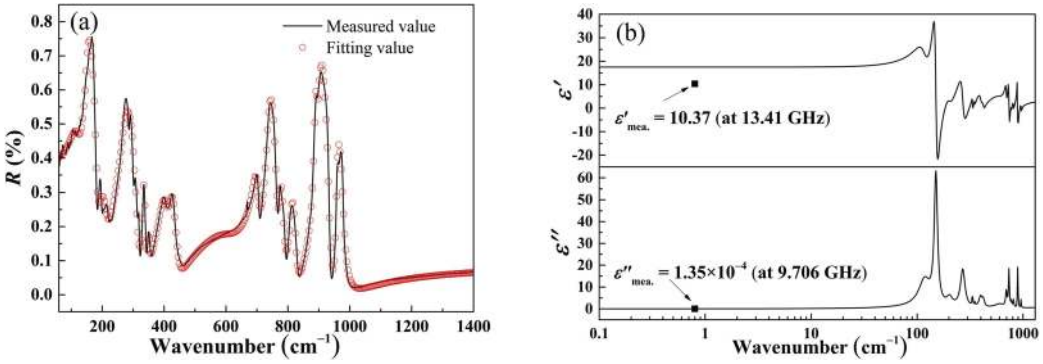

Fig. 11 (a) Measured (black line) and fitted (red line) infrared reflectivity spectra and (b) real and imaginary parts of the complex permittivity for $Ce_2[Zr_{0.94}(Mg_{1/3}Sb_{2/3})_{0.06}]_3(MoO_4)_9$ ceramic sintered at 725 ℃ for 6 h.

Table 8 Phonon parameters after fitting of the $Ce_2[Zr_{0.94}(Mg_{1/3}Sb_{2/3})_{0.06}]_3(MoO_4)_9$ sample sintered at 725 ℃ for 6 h

Mode	$Ce_2[Zr_{0.94}(Mg_{1/3}Sb_{2/3})_{0.06}]_3(MoO_4)_9$ ε_∞ = 2.85				Mode	$Ce_2[Zr_{0.94}(Mg_{1/3}Sb_{2/3})_{0.06}]_3(MoO_4)_9$ ε_∞ = 2.85			
	ω_{oj}	ω_{pj}	γ_j	$\Delta\varepsilon_j$		ω_{oj}	ω_{pj}	γ_j	$\Delta\varepsilon_j$
1	118.72	225.22	35.46	3.60	9	602.91	412.83	155.98	0.47
2	150.75	341.96	12.89	5.15	10	695.94	338.65	22.47	0.24
3	202.86	162.23	31.95	0.64	11	736.26	462.78	17.08	0.40
4	270.42	386.82	31.62	2.05	12	774.75	178.17	15.75	0.05
5	333.43	104.55	6.68	0.10	13	811.10	228.68	18.10	0.08
6	350.41	60.52	5.92	0.03	14	888.05	388.88	7.79	0.19
7	398.23	259.20	34.10	0.42	15	898.43	238.71	12.23	0.07
8	422.68	169.58	22.11	0.16	16	957.54	192.66	9.89	0.04

calculated value (2.68×10^{-4}) of the dielectric loss remained in the same order of magnitude. Both the fitted and measured values correspond well, which indicate that in the microwave frequencies, the dielectric polarization is mainly caused by absorption of phonons in the infrared region [31–33].

4 Conclusions

$Ce_2[Zr_{1-x}(Mg_{1/3}Sb_{2/3})_x]_3(MoO_4)_9$ (x = 0.02, 0.04, 0.06, 0.08, and 0.10) ceramics were fabricated well via the traditional solid-state method. The pure-phase with space group of $R\bar{3}c$ was detected for all specimens. The dense microstructure and clear grain boundary of specimens can be observed in SEM photos. The crystal structures were investigated deeply by the Rietveld refinement method. The ε_r, $Q\times f$, and τ_f values of these samples were strongly dependent on chemical bonds such as $f_{i(Mo1–O(2))}$, $U_{(Zr(Mg/Sb)1–O(4))}$, and $E_{(Mo1–O(1))}$, respectively. The infrared reflectivity spectra were in good agreement with the dielectric properties of samples. Meanwhile, $Ce_2[Zr_{0.94}(Mg_{1/3}Sb_{2/3})_{0.06}]_3(MoO_4)_9$ ceramic with ε_r = 10.37, $Q\times f$ = 71,748 GHz, and τ_f = −13.6 ppm/℃ was obtained at 725 ℃ for 6 h.

Acknowledgements

This work was supported by the National Natural Science Foundation (No. 51972143). The authors would like to thank the administrators in infrared beamline workstation of National Synchrotron Radiation Laboratory (NSRL) for the help in infrared measurement.

References

[1] Guo HH, Zhou D, Liu WF, *et al*. Microwave dielectric properties of temperature-stable zircon-type (Bi,Ce)VO_4 solid solution ceramics. *J Am Ceram Soc* 2020, **103**: 423–431.

[2] Zheng JJ, Yang YK, Wu HT, *et al*. Structure, infrared spectra and microwave dielectric properties of the novel Eu_2TiO_5 ceramics. *J Am Ceram Soc* 2020, **103**: 4333–4341.

[3] Li CC, Yin CZ, Deng M, *et al*. Tunable microwave dielectric properties in SrO–V_2O_5 system through compositional modulation. *J Am Ceram Soc* 2020, **103**: 2315–2321.

[4] Bi JX, Xing CF, Yang CH, *et al*. Phase composition, microstructure and microwave dielectric properties of rock salt structured Li_2ZrO_3–MgO ceramics. *J Eur Ceram Soc* 2018, **38**: 3840–3846.

[5] Pang LX, Zhou D. Modification of $NdNbO_4$ microwave dielectric ceramic by Bi substitutions. *J Am Ceram Soc* 2019, **102**: 2278–2282.

[6] Yin CZ, Li CC, Yang GJ, *et al*. $NaCa_4V_5O_{17}$: A low-firing microwave dielectric ceramic with low permittivity and chemical compatibility with silver for LTCC applications. *J Eur Ceram Soc* 2020, **40**: 386–390.

[7] Tao BJ, Wang WF, Liu HY, *et al*. Low-temperature sintering LiF-doped $Li_4Mg_3[Ti_{0.6}(Mg_{1/3}Nb_{2/3})_{0.4}]_2O_9$ microwave dielectric ceramics for LTCC applications. *Ceram Int* 2021, **47**: 2584–2590.

[8] Guo HH, Zhou D, Pang LX, *et al*. Microwave dielectric properties of low firing temperature stable scheelite structured (Ca,Bi)(Mo,V)O_4 solid solution ceramics for LTCC applications. *J Eur Ceram Soc* 2019, **39**: 2365–2373.

[9] Liu WQ, Zuo RZ. Low temperature fired $Ln_2Zr_3(MoO_4)_9$ (Ln = Sm, Nd) microwave dielectric ceramics. *Ceram Int* 2017, **43**: 17229–17232.

[10] Zhang YH, Sun JJ, Dai N, *et al*. Crystal structure, infrared spectra and microwave dielectric properties of novel extra low-temperature fired $Eu_2Zr_3(MoO_4)_9$ ceramics. *J Eur Ceram Soc* 2019, **39**: 1127–1131.

[11] Zhang YH, Wu HT. Crystal structure and microwave dielectric properties of $La_2(Zr_{1-x}Ti_x)_3(MoO_4)_9$ ($0 \le x \le 0.1$) ceramics. *J Am Ceram Soc* 2019, **102**: 4092–4102.

[12] Tao BJ, Xing CF, Wang WF, *et al*. A novel $Ce_2Zr_3(MoO_4)_9$ microwave dielectric ceramic with ultra-low firing temperature. *Ceram Int* 2019, **45**: 24675–24683.

[13] Zheng JJ, Liu YH, Tao BJ, *et al*. Crystal structure and optimised microwave dielectric properties of $Ce_2(Zr_{1-x}Ti_x)_3(MoO_4)_9$ solid solutions. *Ceram Int* 2021, **47**: 5624–5630.

[14] Xiao M, He SS, Meng J, *et al*. Bond ionicity, lattice energy, bond energy and the microwave dielectric properties of non-stoichiometric $MgZrNb_{2+x}O_{8+2.5x}$ ceramics. *Mater Chem Phys* 2020, **242**: 122412.

[15] Wu ZJ, Meng QB, Zhang SY. Semiempirical study on the valences of Cu and bond covalency in $Y_{1-x}Ca_xBa_2Cu_3O_{6-y}$. *Phys Rev B* 1998, **58**: 958–962.

[16] Kim SH, Kim ES. Intrinsic factors affecting the microwave dielectric properties of $Mg_2Ti_{1-x}(Mg_{1/3}Sb_{2/3})_xO_4$ ceramics. *Ceram Int* 2016, **42**: 15035–15040.

[17] Pei CJ, Tan JJ, Li Y, *et al*. Effect of Sb-site nonstoichiometry on the structure and microwave dielectric properties of $Li_3Mg_2Sb_{1-x}O_6$ ceramics. *J Adv Ceram* 2020, **9**: 588–594.

[18] Xia WS, Zhang LY, Wang Y, *et al*. Extrinsic effects on microwave dielectric properties of high-Q $MgZrTa_2O_8$ ceramics. *J Mater Sci: Mater Electron* 2016, **27**: 11325–11330.

[19] Silverman BD. Microwave absorption in cubic strontium titanate. *Phys Rev* 1962, **125**: 1921–1930.

[20] Xue DF, Zhang SY. Calculation of the nonlinear optical coefficient of the $NdAl_3(BO_3)_4$ crystal. *J Phys: Condens*

Matter 1996, **8**: 1949–1956.
[21] Berkov DV. Evaluation of the energy barrier distribution in many-particle systems using the path integral approach. *J Phys: Condens Matter* 1998, **10**: L89–L95.
[22] Levine BF. Bond susceptibilities and ionicities in complex crystal structures. *J Chem Phys* 1973, **59**: 1463–1486.
[23] Zhang P, Zhao YG, Wang XY. The correlations between electronic polarizability, packing fraction, bond energy and microwave dielectric properties of $Nd(Nb_{1-x}Sb_x)O_4$ ceramics. *J Alloys Compd* 2015, **644**: 621–625.
[24] Zhang P, Zhao YG. Effects of structural characteristics on microwave dielectric properties of $Li_2Mg(Ti_{1-x}Mn_x)_3O_8$ ceramics. *J Alloys Compd* 2015, **647**: 386–391.
[25] Sanderson RT. Multiple and single bond energies in inorganic molecules. *J Inorg Nucl Chem* 1968, **30**: 375–393.
[26] Sanderson RT. *Chemical Bonds*, *Bond Energy*. New York (USA): Academic press, 1971.
[27] Sanderson RT. Electronegativity and bond energy. *J Am Chem Soc* 1983, **105**: 2259–2261.
[28] Luo YR. *Comprehensive Handbook of Chemical Bond Energies*. Boca Raton (USA): CRC press, 2007.
[29] Chen Z, Jia H, Sharafudeen K, *et al*. Up-conversion luminescence from single vanadate through blackbody radiation harvesting broadband near-infrared photons for photovoltaic cells. *J Alloys Compd* 2016, **663**: 204–210.
[30] Guo J, Zhou D, Wang L, *et al*. Infrared spectra, Raman spectra, microwave dielectric properties and simulation for effective permittivity of temperature stable ceramics $AMoO_4$–TiO_2 (A = Ca, Sr). *Dalton Trans* 2013, **42**: 1483–1491.
[31] Pang LX, Zhou D, Qi ZM, *et al*. Structure-property relationships of low sintering temperature scheelite-structured $(1-x)BiVO_4$–$xLaNbO_4$ microwave dielectric ceramics. *J Mater Chem C* 2017, **5**: 2695–2701.
[32] Liu LT, Chen YG, Feng ZB, *et al*. Crystal structure, infrared spectra, and microwave dielectric properties of the $EuNbO_4$ ceramic. *Ceram Int* 2021, **47**: 4321–4326.
[33] Li JM, Zhang CM, Liu H, *et al*. Structure, morphology, and microwave dielectric properties of $SmAlO_3$ synthesized by stearic acid route. *J Adv Ceram* 2020, **9**: 558–566.